

A Two-phase Weakly Compressible Smoothed Particle Hydrodynamics Study of Wave-structure Interaction with Several Benchmark Numerical Validations in Oceanographic Engineering

Zhenyu Ouyang¹, Boo Cheong Khoo^{1,a)}, Damodaran Murali¹

¹ *Department of Mechanical Engineering, National University of Singapore, Singapore 117575*

Abstract

A two-phase particle hydrodynamics (SPH) method is employed to study a wave-structure interaction problem in a wave tank and several benchmark cases in oceanographic engineering are validated. The two-phase dam breaking is first tested, and the results are compared to those of one-phase and experimental data. It is found that two-phase simulation forms a cavity with a smoother interface, due to the local anti-extrusion of the air phase. Afterwards, a “mirror” open boundary condition is validated to be robust and accurate by simulating a flow past a two-dimensional cylinder. This open boundary is then implemented in the top and left sides of a two-phase wave tank, with a piston to generate second-order regular wave. It is observed that, compared to the one-phase simulation, the two-phase one can obtain a smoother water free surface and prevent the nonphysical water splash when interacting with the sloped dissipative beach. This tank is also used to investigate the wave-structure interaction problems by setting a fixed rigid structure below the wave surface and a freely floating box on the wave surface. For the fixed rigid structure case, a typical wave-structure interaction period is captured and described using pressure contours and velocity vectors at three representative instants. Increasing the structure height, the wave height after the structure decreases, yet no evident variations are found when changing the structure thickness. For the freely floating box case, our results (the movement of the box) show an agreement with the existing experimental data.

^{a)} Email address for correspondence: mpekbc@nus.edu.sg

1. Introduction

The wave-structure interaction (WSI) problem, one or multiple solid structures interacting with an internal or surrounding fluid flow, is one of the most significant and fundamental problems in oceanographic engineering. For instance, the breakwaters and seawalls, two widely used coastal structures to enable safe navigation into harbors, providing calm water areas for loading and unloading of ships and protect the shore, are suffering from the shock of the ocean waves at any moment [1-3]. The floating structure, e.g., the huge ship or the offshore platform on the ocean under the wind and wave loads, is another typical example where WSI has an important impact on the its safety and stability [4]. Recently, the very large floating structures (VLFS) for coastal and offshore uses have increased significantly due to the demand for developable land around the coastal cities [5-6]. The durability and resistance to fatigue, one of the key concepts in material selection, design and manufacturing of VLFS, are dominated by the local ocean wave loads, strength and period.

The WSI is essentially a fluid structure interaction (FSI) problem, in which a comprehensive study remains a challenge due to their strong nonlinearity and multidisciplinary nature [7-8]. Since the analytical solutions to the governing equations are impossible to obtain for most of the problems and laboratory experiments are limited in scope, numerical simulation may usually be a feasible way to investigate the fundamental physics involved in the complex interaction between fluids and solids with the advances of computer technology and improvements of simulation algorithms. For instance, an efficient numerical algorithm has been used to investigate the interaction between the water wave and the motion of the boat with a speed that has outpaced the availability of testing data and existing design methods [9-10]. The numerical procedures to solve the FSI problems may be broadly classified into two approaches, i.e., the monolithic approach and the partitioned approach [11]. The monolithic approach [12-13] treats the fluid and structure dynamics in a uniform framework to form a single governing equation for solving the entire problem

simultaneously, and the interfacial conditions are implicit in the solution procedure. This approach can achieve a more accurate result compared to the partitioned one, but at the cost of more computing resources and the difficulties in establishing and implementing the models. The partitioned approach treats the fluid and the structure separately with their respective numerical schemes, and communicates the information between the fluid and structure explicitly. Another classification of the FSI numerical methods is based on whether the mesh exists or not. The sophisticated mesh approaches, including the finite element method (FEM) [14-15], finite volume method (FVM) [16-17] and the lattice Boltzmann method (LBM) [18-22], are widely employed to cope with the FSI problems using the conforming mesh or non-conforming mesh. The conforming mesh method uses the real mesh nodes to capture the moving or the deforming of a structure, in which the reconstruction of the mesh is required. In non-conforming mesh method, on the other hand, the fluid and solid equations can be solved in their respective grids and exchanging the information through an interpolation process. For the meshless methods, the dissipative particle dynamics (DPD) and the smoothed particles hydrodynamics (SPH) are two kinds of popular methods which are widely adopted to investigate the multiphase flows [23-28], biological flows[29-30] and the FSI problems[31-32], due to the inherent merits (the particle-based properties) in handling moving interfaces, large deformation or free surface problems. In the present study, a SPH method is employed to study the WSI problem, and we have also conducted some benchmark tests to ensure the accuracy of our code.

Though SPH is originally developed for astrophysical applications [33-34], it has been extended to model wave generation and WSI problems [35-39]. Ni and Feng [35] have presented a 2D numerical wave tank based on an open-source SPH-based *DualSPHysics* model, using a source generation and absorption technology with analytical relaxation approach. They use a generation zone instead of moving boundaries to obtain the wave based on the Stokes wave theory. Their work is limited to the regular wave cases and no second-order bound long waves are considered. Wen

et al. [36] have implemented an absorbing wavemaker in *DualSPHysics* although the wave generation is only based on linear wave theory and the presented results only focus on regular wave tests. Recently, a long-crested wave generation and absorption models are implemented in *DualSPHysics* by Altomare et al. [37] to investigate second-order long-crested monochromatic and random waves. They use moving boundaries to mimic the action of a piston-type wavemaker. These implementations have been validated with theoretical solutions and experimental results, in terms of water surface elevation, wave orbital velocities, wave forces and capacity for damping the re-reflection inside the fluid domain. For the WSI problems, Meringolo et al. [38] have proposed a 2D diffusive weakly compressible SPH model to simulate wave loads and hydraulic characteristics at perforated breakwaters. They investigate the interaction between regular waves with fully and partially perforated breakwaters and the results are successfully compared with the experimental data in terms of dynamic pressures acting on the body profiles of the considered breakwater and wave reflection. Lately, a coupled finite particle method (FPM) which combines the advantages of FPM, SPH, δ -SPH model and particle shifting technology (PST) is proposed to model WSI [39]. The Oscillating Wave Surge Converter (OWSC) including two-dimensional (2D) and three dimensional (3D) simulations are conducted successfully using this method. The interaction between the wave or the water with a flexible structure has also attracted researchers' attention using SPH. Antoci et al. [32] have proposed a Lagrangian SPH model to investigate the deformation of an elastic gate subjected to time-dependent water pressure. The horizontal and vertical displacements of the free end of the gate and the water level are compared well with their experiment data. Afterwards, the dam-break flow impacting on the flexible structures problem has been considered using an improved SPH combined with element bending group (EBG) method [40]. The good agreement of numerical results with existing experimental and numerical results clearly demonstrates the effectiveness of the SPH and EBG coupling approach in modeling fluid-flexible structure interactions.

These researches aforementioned mainly focus on one-phase simulation where the air phase is neglected. In the present study, the two-phase simulations of dam breaking, the wave maker in a tank and the WSI are investigated in the framework of SPH. The “mirror” open boundary condition is validated firstly and then applied to the wave maker tank and WSI problems to deal with zero velocity or pressure gradients of the air phase. This paper aims to understand the physics of several typical cases related to the oceanographic engineering using two-phase simulation, as well as to reveal a typical interaction process between the regular wave and the rigid structure and freely floating box. Our work is also a preparation for the more complex simulations of oceanographic engineering in the nearly future.

2. Description of the SPH model

2.1 The governing equations and SPH scheme

The continuity and the momentum conservation equations of a weakly compressible flow can be written as

$$\frac{D\rho}{Dt} = -\rho \nabla \cdot \mathbf{u}, \quad (1)$$

$$\frac{D\mathbf{u}}{Dt} = \frac{1}{\rho} \nabla \cdot \boldsymbol{\sigma} + \mathbf{f}, \quad (2)$$

where \mathbf{u} and ρ are respectively, the velocity and the density of the fluid. \mathbf{f} is an acceleration resulting from an external force. $\boldsymbol{\sigma}$ is the stress tensor including the pressure gradient term and the viscosity term. In the framework of SPH, the corresponding discretized form of the continuity Eq. (1) can be written as

$$\left\{ \frac{D\rho}{Dt} \right\}_i = \rho_i \sum_j \frac{m_j}{\rho_j} \mathbf{u}_{ij} \cdot \nabla_i W_{ij} + \delta_i, \quad (3)$$

where W is the smoothing kernel function. Note that $\nabla_i W_{ij} = \partial W_{ij} / \partial x_i$, the additional term δ_i is introduced to improve the stability of the SPH numerical calculation [41] and to remove spurious pressure oscillations which can exist in weakly-compressible SPH. Note that the vector \mathbf{u}_{ij} denotes the difference of \mathbf{u}_i and \mathbf{u}_j . For the momentum conservation equation, a discretized form which is widely used to deal with one- and

two-phase flows, is adopted here [42], it reads,

$$\left\{ \frac{D\mathbf{u}}{Dt} \right\}_i = -\frac{1}{m_i} \sum_j \left(P_i \left(\frac{m_i}{\rho_i} \right)^2 + P_j \left(\frac{m_j}{\rho_j} \right)^2 + \Pi_{ij} \right) \cdot \nabla_i W_{ij} + \sum_j m_j \left(\frac{2\mu \mathbf{r}_{ij} \cdot \nabla_i W_{ij}}{\rho_i \rho_j |\mathbf{r}_{ij}|} \mathbf{u}_{ij} \right) + \mathbf{g}, \quad (4)$$

in which P_i and P_j are respectively the pressures of particle i and particle j ; \mathbf{r}_{ij} denotes the vector from particle i to particle j ; μ is the dynamic viscosity of the fluid. Π_{ij} is the artificial viscosity to alleviate pressure oscillations caused by particles' unphysical concentration and can be described as [43]

$$\Pi_{ij} = \begin{cases} \frac{-\alpha \overline{c_{ij}} \mu_{ij}}{\overline{\rho_{ij}}} & \mathbf{u}_{ij} \cdot \mathbf{r}_{ij} < 0 \\ 0 & \mathbf{u}_{ij} \cdot \mathbf{r}_{ij} \geq 0 \end{cases}, \quad (5)$$

$$\mu_{ij} = \frac{h \mathbf{u}_{ij} \cdot \mathbf{r}_{ij}}{|\mathbf{r}_{ij}|^2 + \eta^2}, \quad (6)$$

where $\overline{\rho_{ij}}$ and $\overline{c_{ij}}$ are respectively the average values of the density and sound speed of particle i and j , h is the smoothing length and $\eta=0.1h$; α is a parameter set according to the characteristic of specific problem. A proper value of α should not be too large which may lead to large error, and should not be too small which may ineffective in alleviating the oscillations in dynamic problems. For the weakly compressible flow, an equation of state commonly used in SPH which relates the pressure to small variations of fluid density can be described as

$$P = B \left(\left(\frac{\rho}{\rho_0} \right)^{\gamma_0} - 1 \right), \quad (7)$$

in which B is the reference pressure, $B = \rho_0 c^2 / \gamma$, ρ_0 is the fluid reference density, c is the speed of sound in the fluid and $\gamma_0 = 7$ is used here. A proper value of B is chosen to ensure that the numerical Mach number is small and compressibility is negligible [44].

2.2 Boundary condition

2.2.1 Wall boundary condition

In this work, the method proposed by Adami *et al.* [45] is adopted to impose no-slip or free-slip boundary conditions on the solid walls. By extrapolating from the

neighboring fluid particles, the pressure on the solid boundary is obtained as

$$P_i = \frac{\sum_j (P_j + (\mathbf{g}_j \cdot \mathbf{r}_{ij}) \rho_j) W_{ij}}{\sum_j W_{ij}}. \quad (8)$$

Once the pressure on the solid boundary is obtained, its corresponding densities can be updated based on Eq. (7).

2.2.2 Open boundary condition

In the SPH, the open boundary condition is usually implemented on the inlet or outlet of the flow with zero velocity or pressure gradients. Without the complete support domains of the fluid particles, severe numerical errors may occur in this area. Recently, a versatile open boundary condition has developed by Tafuni et al. [46], in which a buffer layer is introduced to cope with this problem. The width of the layer usually equals to the support domain radius, and the particles in the area are called ghost particles. For the inlet ghost particles, the velocity is prescribed based on the flow problem and the density is interpolated from the fluid or ghost particles. For the outlet ghost particles, both the velocity and the density are interpolated from the fluid or ghost particles. Taking the outflow open boundary condition as an example, as indicated in Fig. 1, the ghost particles are mirrored with respect to the outlet threshold for the density and velocity interpolations, then the physical quantities of mirror particles are projected back to the corresponding ghost particles using the first-order Taylor series expansion. To restore the consistency of the kernel function [47], the following interpolating schemes are adopted to obtain R_m and $R_{m,\beta}$, which respectively denote the approximation of the physical quantities of mirror particles and their first-order spatial derivatives,

$$R_m = \left| \begin{array}{cc} \sum_j R_j V_j W_{mj} & \sum_j (x_j^\beta - x_m^\beta) V_j W_{mj} \\ \sum_j R_j V_j W_{mj,\gamma} & \sum_j (x_j^\beta - x_m^\beta) V_j W_{mj,\gamma} \end{array} \right| \bigg/ \left| \begin{array}{cc} \sum_j V_j W_{mj} & \sum_j (x_j^\beta - x_m^\beta) V_j W_{mj} \\ \sum_j V_j W_{mj,\gamma} & \sum_j (x_j^\beta - x_m^\beta) V_j W_{mj,\gamma} \end{array} \right|, \quad (9)$$

$$R_{m,\beta} = \frac{\left| \begin{array}{cc} \sum_j V_j W_{mj} & \sum_j R_j V_j W_{mj} \\ \sum_j V_j W_{mj,\gamma} & \sum_j R_j V_j W_{mj,\gamma} \end{array} \right|}{\left| \begin{array}{cc} \sum_j V_j W_{mj} & \sum_j (x_j^\beta - x_m^\beta) V_j W_{mj} \\ \sum_j V_j W_{mj,\gamma} & \sum_j (x_j^\beta - x_m^\beta) V_j W_{mj,\gamma} \end{array} \right|}, \quad (10)$$

where m denotes the mirror particles, and j represents the fluid or ghost particle inside the support domain of particle m . β and γ are the dimension indexes repeated from 1 to 2 or 3. $W_{mj,\gamma} = \partial W_{mj} / \partial x^\gamma$ is the spatial derivative of the kernel function. The first-order Taylor series expansion is,

$$R_{n_0} = R_m + (x_{n_0}^\beta - x_m^\beta) R_{m,\beta}, \quad (11)$$

where n_0 denotes the ghost particles corresponding to the mirror particle m .

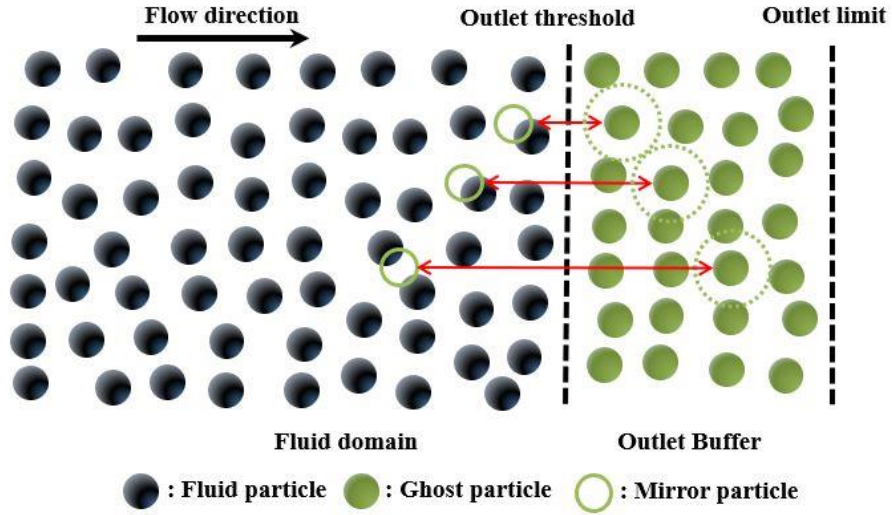


Fig.1 Schematic of the open boundary condition for the outlet

2.3 Time integration schemes

A velocity-Verlet scheme [45,48] is adopted here for the time integration,

$$\mathbf{u}^{n+\frac{1}{2}} = \mathbf{u}^n + \frac{D\mathbf{u}^n}{Dt} \frac{\Delta t}{2}, \quad (12)$$

$$\mathbf{r}^{n+\frac{1}{2}} = \mathbf{r}^n + \mathbf{u}^{n+\frac{1}{2}} \frac{\Delta t}{2}, \quad (13)$$

$$\rho^{n+1} = \rho^n + \frac{D\rho^{n+\frac{1}{2}}}{Dt} \Delta t, \quad (14)$$

$$\mathbf{r}^{n+1} = \mathbf{r}^{n+\frac{1}{2}} + \mathbf{u}^{n+\frac{1}{2}} \frac{\Delta t}{2}, \quad (15)$$

$$\mathbf{u}^{n+1} = \mathbf{u}^{n+\frac{1}{2}} + \frac{D\mathbf{u}^{n+1}}{Dt} \frac{\Delta t}{2}. \quad (16)$$

Using the mid-point velocity, the force has to be performed only once per timestep to obtain the particle acceleration. To obtain a proper step size, several criteria [43] should be satisfied at the same time for the stability reasons. Here, we consider the CFL-condition which is based on the smoothing length h , the maximum sound speed c_{max} , the maximum flow speed \mathbf{u}_{max} , the viscosity ν as well as the body force \mathbf{g} ,

$$\Delta t \leq 0.25 \frac{h}{c_{max} + |\mathbf{u}_{max}|}, \quad (17)$$

$$\Delta t \leq 1.25 \frac{h^2}{\nu}, \quad (18)$$

$$\Delta t \leq 0.25 \left(\frac{h}{|\mathbf{g}|} \right)^{\frac{1}{2}}. \quad (19)$$

3. Numerical Results and Discussion

3.1 Two-phase dam breaking

Two-phase dam breaking is a significant benchmark case which contains several hydrodynamic phenomena, including surface break-up, water jet and impact pressure. It is also a multiphase flow with a very large density difference, and hence an ideal case in validating the accuracy and stability of the SPH code. As indicated in Fig.2, the height and length of the computational domain are respectively 1.6m and 0.5m. The water phase, with $L=0.6\text{m}$ in length and $H=0.3\text{m}$ in height and a reference density of 1000kg/m^3 , is released from stillness. The other area is occupied by air with a reference density of 1.29kg/m^3 , which corresponds a very high density-ratio (water / air). In this work, for the two-phase flow with a resolution $R=0.0025$ m, the

corresponding total particle number N equals to 158916. The smoothing length is set to $h=1.5R$. The laminar viscosity is usually could be ignored [49] in this problem, and the parameter of the artificial term $\alpha=0.05$. A fixed computational time step is set to 5×10^{-5} s for this problem.

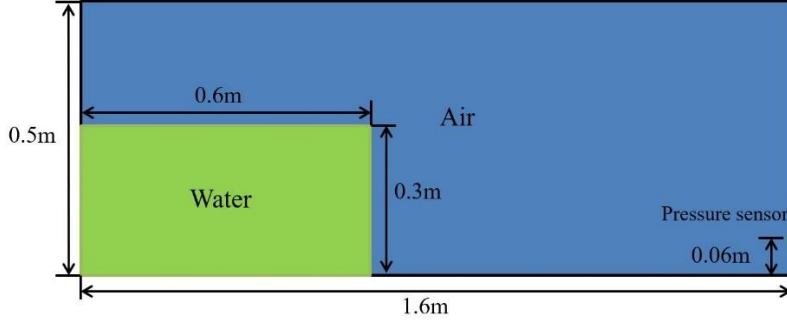


Fig. 2 Schematic of a multiphase dam break.

The dam breaking flow snapshots of one- and two-phase SPH modeling are compared with the two-phase result of Chen et al. [50] at a dimensionless instant $t(g/H)^{0.5}=6.4$ as indicated in Fig.3. It is found that, after impacting the vertical wall, the water reaches a relatively higher level than that of the reference [50]. Apart from the area where the air bubble entrapped by the backward plunging breaker, the water outline of the one-phase flow is almost coincident with that of the two-phase one. It is observed that the two-phase simulation forms a smoother interface of cavity, due to the anti-extrusion of the air phase there. Figure 4 displays the pressure comparison of the two-phase flows between the results from reference [50], the pressure distribution of our simulation at the instant is similar to that of the reference [50] in spite of a slightly larger value for our result especially in the vicinity of the walls. The splashed water with uneven distribution may be affected by the higher pressure (compared to that of the reference [50]). Note that the pressure below the cavity is comparatively larger than that acting on the cavity top, this pressure difference leads to the collapse of the cavity for the one-phase flow without the anti-extrusion of the air (see Fig.3 and Fig.4).

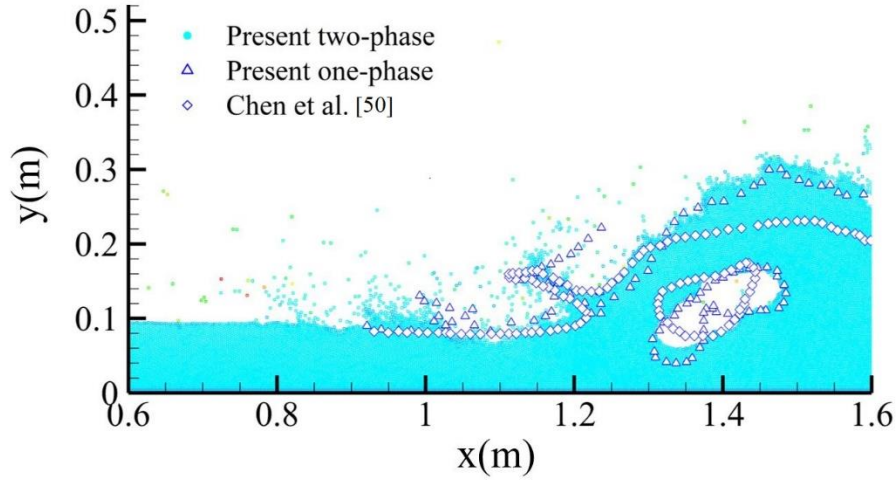


Fig. 3 Comparison of one- and two-phase SPH results with that of Chen et al. [50] for dam breaking flow at dimensionless time $t(g/H)^{0.5}=6.4$. (The resolution of the present simulations uses $R=0.0025\text{m}$)

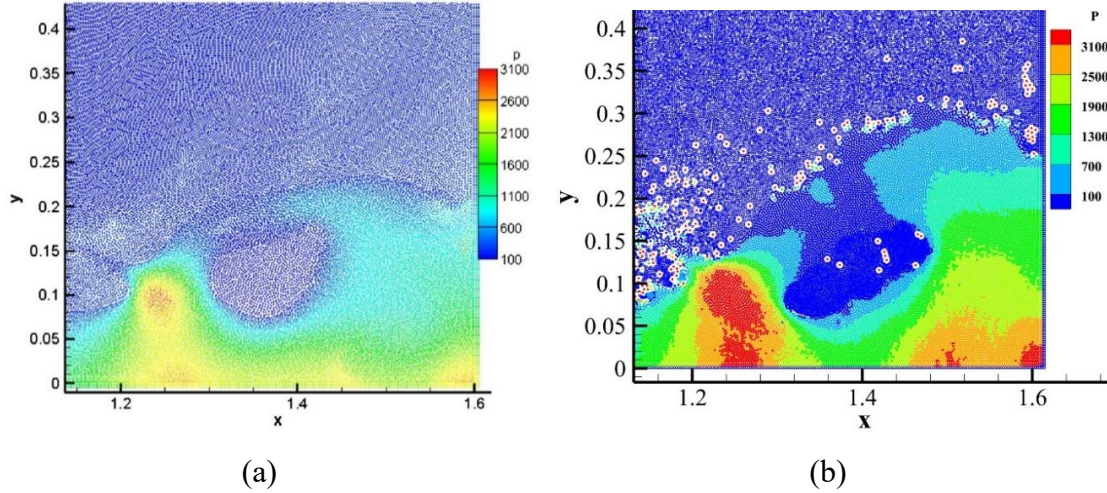


Fig. 4 Comparison of pressure for two-phase SPH simulation of dam breaking flow at dimensionless time $t(g/H)^{0.5}=6.4$. (a) The result of Chen et al. [50] (b) Present study. (The resolution of present simulations uses $R=0.0025\text{m}$)

Figure 5 shows the pressure evolution of the sensor as indicated in Fig. 2. Two resolutions ($R=0.005\text{m}$ and 0.0025m) are presented for the convergence test, it is found that resolution enhancement (to 0.0025m) only smooths the pressure curve rather than affect the averaged pressure. In our simulations, we adopt the resolution of 0.0025m which has also been employed by Chen et al. [50] compromising between the accuracy and computing resources. Compared to the experimental data of Colagrossi & Landrini [51], it is observed that our numerical models give a reliable prediction of the pressure evolution. The pressure of the two-phase simulation lags a little from the one-phase result in time scale, which is due to the compression of the

surrounding air. The pressure peak of the sensor in our simulation appears at approximate dimensionless instant 6.4 when backward plunging breaker entrapping the air and creating the cavity, in which the vertical wall is suffering the most powerful impact in forcing the water to return. After that, the violent water gradually restores till the vertical wall only suffers hydrostatic pressure.

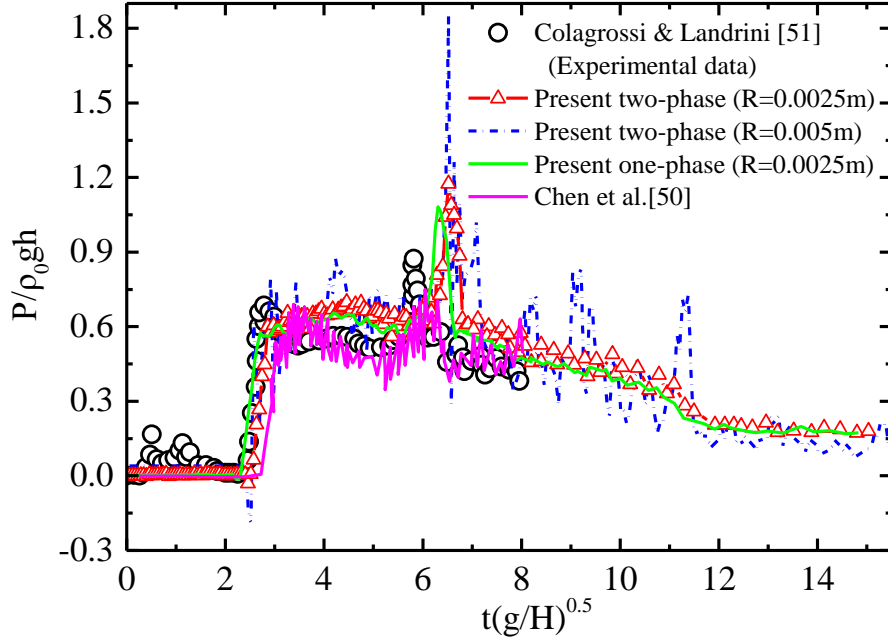


Fig. 5 Comparison of the time variations of dimensionless pressure.

3.2 Flow past a cylinder

Flow past a circular cylinder is validated to test the effectiveness of the open boundary condition which will be implemented in the following investigations. This problem presents many numerical and experimental solutions [46,52-54]. Compared with the mesh-based method, the open boundary of SPH is still an open research point due to the Lagrangian properties of particle method [55]. In the present study, a “mirror” open boundary which introduced in Section 2.2.2 is adopted here to model the inlet, outlet and the infinite far field boundary conditions. As indicated in Fig. 6, the buffer 1 and the buffer 2 respectively denote the inlet and the outlet open boundaries using several layers of ghost particles. The thickness of the buffers is set to a support radius of the SPH kernel function. The inlet velocity is prescribed with $U_0=0.2\text{m/s}$, and the diameter of the circular D is set to be the characteristic length, corresponding to 0.1m . The circular object is located with its center $5D$ from the inlet

and discretized by no-slip wall boundary particles as introduced in Section 2.2.1. The circular is surrounded by a viscous fluid filling in a computational domain of dimensions $15D \times 20D$. These dimensions we use have proved to be feasible to minimize boundary effects and avoid a particle convergence study [55]. Two kinds of boundary conditions, including the open boundary and the no-slip solid boundary with a prescribed velocity $U_0=0.2\text{m/s}$, are implemented on the top and bottom walls for comparison in modelling the infinite boundary conditions. The Reynolds number is defined as $Re=U_0 D \rho_0 / \mu$, where μ , ρ_0 are respectively the dynamic viscosity and the reference density 1000kg/m^3 . We validate a steady case ($Re=20$) and an unsteady case ($Re=200$) by varying the dynamic viscosity from $1\text{ Pa}\cdot\text{s}$ to $0.1\text{ Pa}\cdot\text{s}$. The particle resolution is set to $R=0.05D$, and the smoothing length is set equal to $h=1.5R$. Note that the parameter of the artificial term (in Eq. 5) α is set to zero and the real viscosity term in Eq.4 is activated for this problem in which the fluid viscosity can not be neglected. A fixed computational time step is set to $5 \times 10^{-4}\text{ s}$ for this problem.

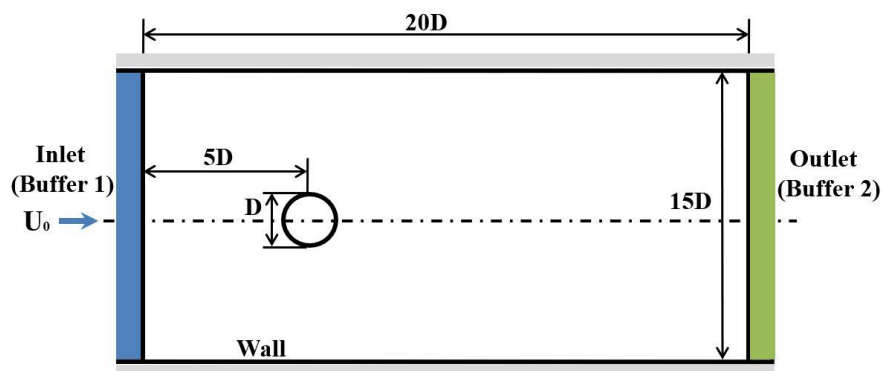


Fig. 6 The Schematic of the 2-D flow past a cylinder (Buffer 1 and Buffer 2 indicate open boundary conditions)

Figures 7-9 display the velocity, pressure and the vorticity contours of the 2D flow past a cylinder at $Re=20$ and 200 . Note that all the physical quantities have been nondimensionalized with the dimensionless velocity $V^*=u/U_0$, the dimensionless pressure $P^*=2P/(\rho_0 U_0^2)$ and the dimensionless vorticity $W^*=\Omega D/U_0$. It is observed that the pressure field calculated for the two representatively Reynolds numbers does not show any discernable spurious oscillations and the periodic vortex shedding is

clearly captured at $Re=200$. To better assess accuracy of our code, the drag and lift coefficients, $C_d=2F_d/(\rho_0 U_0^2 D)$ and $C_l=2F_l/(\rho_0 U_0^2 D)$, are obtained as shown in Fig. 10 (a) and (b), respectively. Here F_d and F_l denote the drag and lift force, respectively. The drag coefficient converges to a steady value of $C_d = 2.28$ for $Re = 20$ and $C_d = 1.42$ for $Re = 200$. A null lift coefficient is observed and expected for the steady case ($Re=20$), and $C_l = 0.655$ for the unsteady case ($Re=200$). Compared with the reference results, it is noted that the lift force of the present study oscillates earlier than that in the reference, this is because the initial velocity of the fluid field is set to 0.2m/s to accelerate the convergence of the calculation whereas that of the reference starts from rest. The vortex shedding frequency f at $Re=200$ is calculated by measuring the period between the passage of a vortex core and a successive one at a given location and taking the inverse. Using the frequency f , the Strouhal number which defined as $St = f D/U_0$, is obtained as indicated in Tab. 1. Our results for Strouhal number, lift and drag coefficient are compared with those in other references, indicating that the “mirror” open boundary condition implemented in our code can accurately cope with open boundary with zero pressure and velocity gradients.

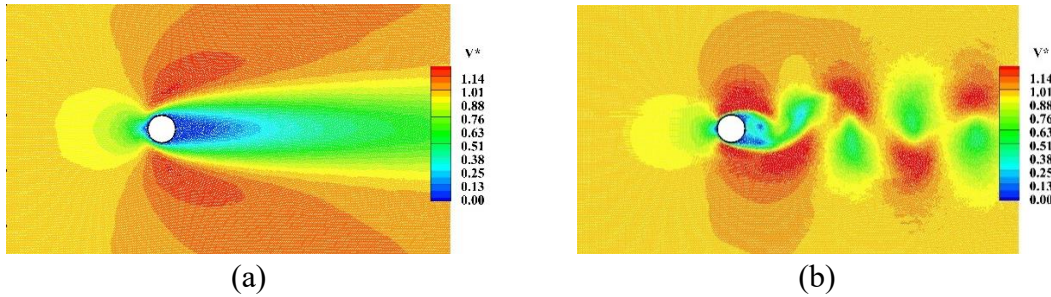


Fig. 7 Velocity contours of the 2D flow past a cylinder. (a) $Re=20$ (b) $Re=200$.

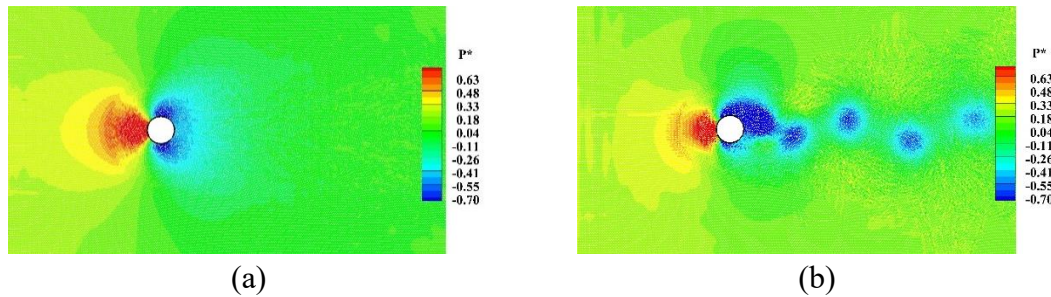


Fig. 8 Pressure contours of the 2D flow past a cylinder. (a) $Re=20$ (b) $Re=200$.

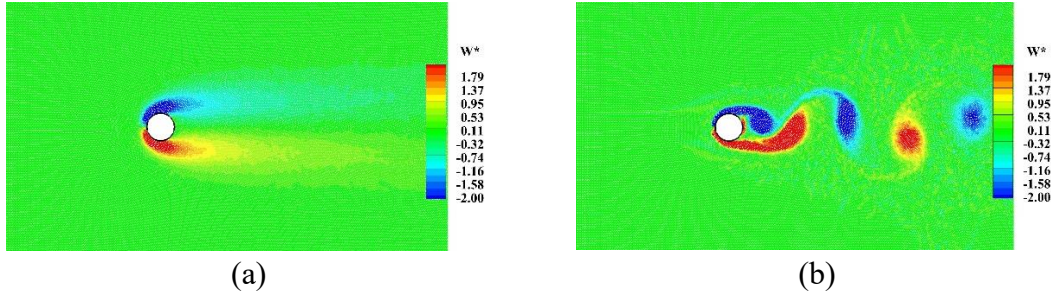


Fig. 9 Vorticity contours of the 2D flow past a cylinder. (a) $Re=20$ (b) $Re=200$.

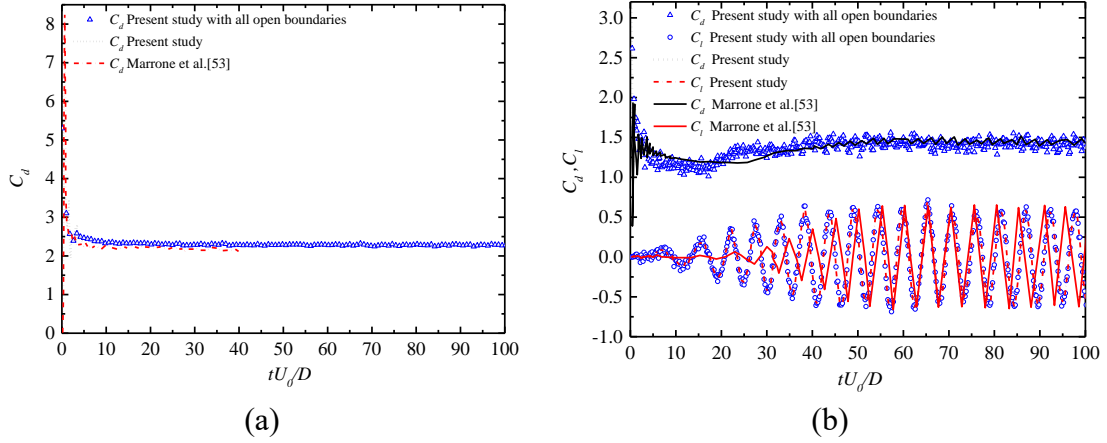


Fig. 10 The drag and the lift force coefficients. (a) $Re=20$ (b) $Re=200$.

Table 1 Comparison of the lift coefficient, drag coefficient and Strouhal number.

	C_l	C_d	St
Present study $Re=20$	-	2.28	-
Tritton [52] $Re=20$	-	2.22	-
Marrone et al. [53] $Re=20$	-	2.20	-
Tafuni et al. [46] $Re=20$	-	2.29	-
Present study $Re=200$	0.655	1.42	0.188
Le et al. [54] $Re=200$	0.676	1.38	0.192
Marrone et al. [53] $Re=200$	0.680	1.38	0.200
Tafuni et al. [46] $Re=200$	0.693	1.46	0.206

3.3 Wave generation in a tank

The two-phase wave generation in a tank is investigated here. Based on the assumptions of irrotational and incompressible fluid and constant pressure at the free surface, the Biesel transfer function could be used to describe the relation between wave amplitude and wavemaker displacement [56]. The far-field solution for the free-surface elevation is expressed as

$$\eta_0(x, t) = \frac{H_0}{2} \cos(\omega t - kx + \delta_0), \quad (20)$$

where H_0 is the wave height, $\omega = 2\pi/T$ is the angular frequency, $k = 2\pi/\lambda$ is the wave number with T the wave period and λ the wavelength. The initial phase δ_0 is given by a random number between 0 and 2π . For the piston-type wavemaker, the Biesel transfer function under the hypothesis of monochromatic sinusoidal waves is expressed as

$$\frac{H_0}{S_0} = \frac{2 \sinh^2(kd)}{\sinh(kd) \cosh(kd) + kd}, \quad (21)$$

where S_0 is the piston stroke and d is the water depth. The time series of the piston movement thus is given by

$$e(t) = \frac{S_0}{2} \sin(\omega t + \delta_0). \quad (22)$$

Madsen [57] has developed a simple second-order wave maker theory to generate relatively long second-order Stokes waves that would not change shape as they propagate. To generate the second-order regular wave, an extra term should be added to the Eq.22 for the piston displacement, it reads

$$e(t) = \frac{S_0}{2} \sin(\omega t + \delta_0) + \left[\left(\frac{H_0^2}{32d} \right) \left(\frac{3 \cosh(kd)}{\sinh^3(kd)} - \frac{2S_0}{H_0} \right) \right] \sin(2\omega t + 2\delta_0). \quad (23)$$

In the present study, the second-order Stokes waves are obtained using the piston-type wavemaker, and the computational domain for the 2D two-phase wave tank is shown in Fig. 11. The reference densities of water and air are respectively 1000 kg/m^3 and 1.29 kg/m^3 . The open boundary conditions are implemented on Buffer 1 and Buffer 2 with the initial density equaling to the air density, and the dimensions of the air phase area are respectively set to a height of $d_a = 0.35 \text{ m}$ and a width of $S_a = 0.4 \text{ m}$ (See Fig.11). Regular water waves are propagated along a 6-m-long tank ($a = 1 \text{ m}$) with a 1:5-sloped dissipative beach at the end, in order to absorb the reflected waves. The no-slip boundary conditions are implemented on the bottom wall and the dissipative beach. Wave gauge (WG)1, WG2 and WG3 are the cross sections where

the sensors are set to monitor the wave velocity and the height. The initial water depth d , wave height H_0 , period T and wavelength λ are respectively 0.27 m, 0.1m, 1.3s and 1.89m. Note that in Fig. 6 a rigid structure is set in the water, which is only activated in the next section to consider the WSI problem. In this simulation we use a resolution of $R=0.01\text{m}$ and a smoothing length of $h=1.5R$, corresponding to the total particle numbers of 21900 and 53161 for the one-phase and the two-phase simulations, respectively. The parameter of the artificial term α in Eq. 5 and the computational time step are respectively set to 0.01 and 1×10^{-4} s for this problem.

Figure 12 presents theoretical and our numerical results for the comparison of the free surface elevations at different wave gauges ($x=2\text{m}$ and $x=4\text{m}$) using the piston wave maker. Note that we have also presented the one-phase results using the open SPH resource *DualSPHysics* with the same resolution of $R=0.01\text{m}$. It is found that the results from both our simulations (one-phase and two-phase) and *DualSPHysics* match the theoretical solution to a good extent although the trough of wave is slightly overestimated by SPH, indicating that the wave are properly generated and the effect of the air on the wave elevations seems negligible. Figure 13 presents the comparison of the velocity components between theoretical and our results. Note that the height of the monitored location is 0.12 m ($d_2=0.12\text{m}$) in the WG1 profile. Apart from the horizontal velocity which is slightly underestimated at the peak, our results could provide a satisfactory accuracy. The horizontal velocity contours for one-phase and two-phase wave generation problems at $t=16\text{s}$ are shown in Fig. 13. Note that in Fig. 13 (b), the air particles are not displayed. It is noticed that the same velocity patterns and free-surface profiles are observed for the two approaches in a global sight. When focusing on the sloped dissipative beach area as indicated in Fig. 13 (c) and (d), it is found that the water particles of the one-phase simulation splash more severely than those of the two-phase simulation, indicating that the air phase could smooth the water-air interface by complementing the particles for the calculation in the vicinity of the water surface area where the particle supporting domain is truncated for the one-phase problem. Figure 15 shows the snapshot of the density for two-phase wave

generation study at $t=16s$. The air phase and water phase can be clearly distinguished due to the huge density difference. In the vicinity of the wave crest as indicated in Fig.15 (c), the velocities of the air phase and the water phase form a circular vector field with head and tail connected, indicating the continuity of velocity at the air-water interface.

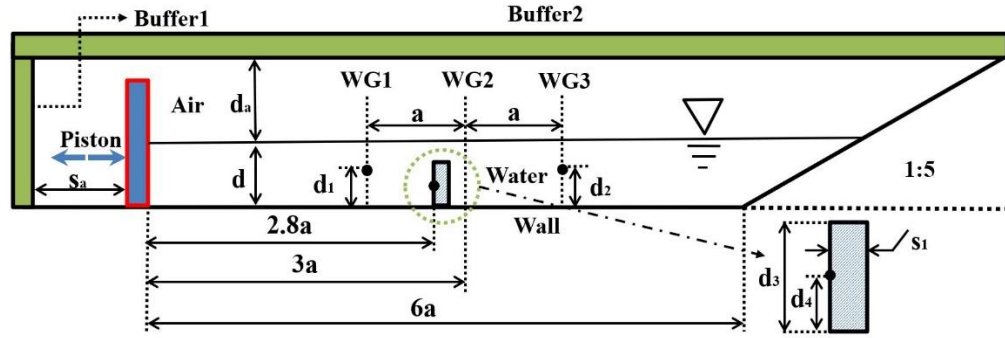


Fig. 11 Schematic of computational domain for the 2D wave tank.

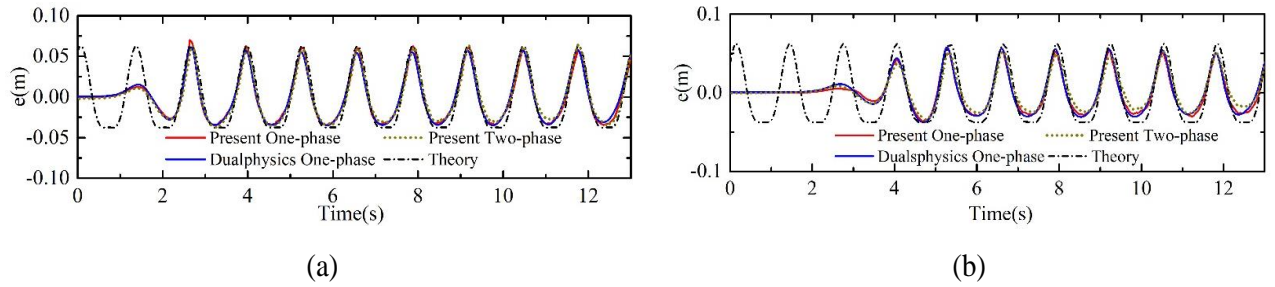


Fig. 12 Comparison of theoretical and numerical free surface elevations at different wave gauges for the wave generation study. (a) $x=2m$ (b) $x=4m$

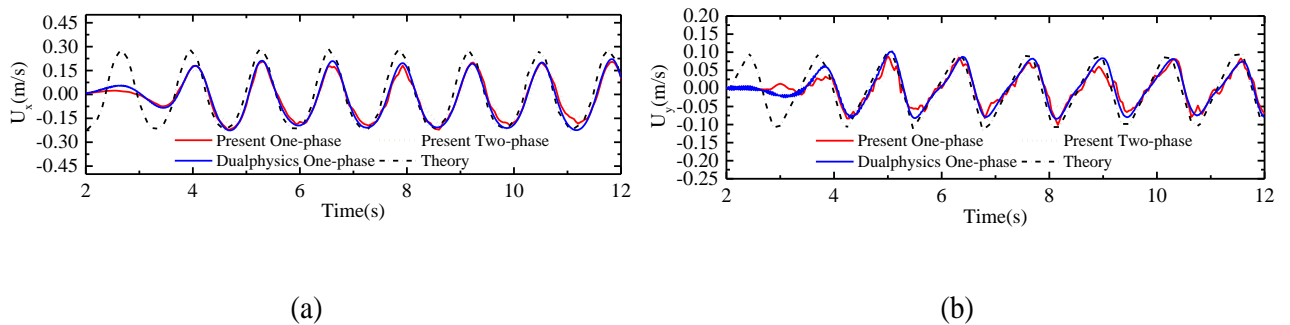


Fig. 13 Comparison of theoretical and numerical orbital velocities at the velocity gauge ($x=4m, d_2=0.12m$) for the wave generation study. (a) U_x (b) U_y

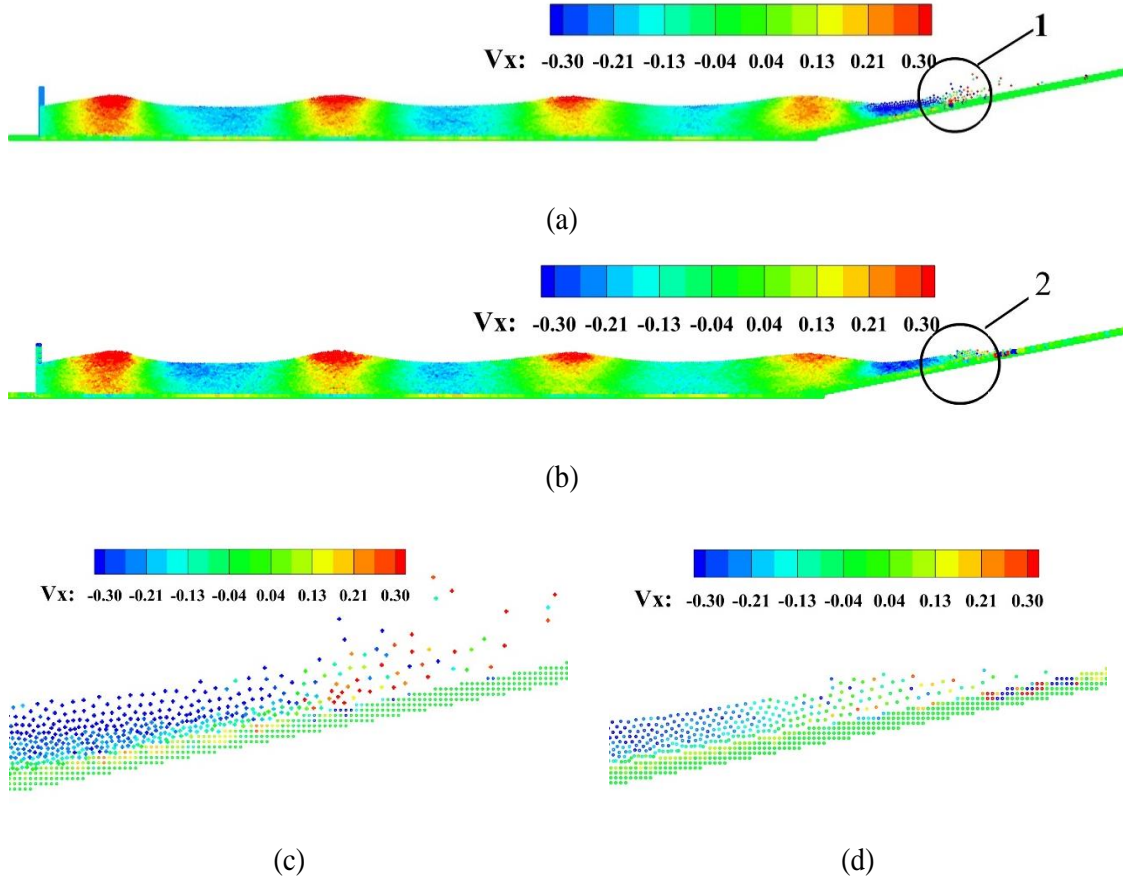


Fig. 14 Snapshot of the horizontal velocity component for one-phase and two-phase wave generation studies at $t=16s$. (a) One-phase (b) Two-phase. Here (c) and (d) correspond to the enlarged of (a) and (b) at marked 1 and marked 2, respectively.

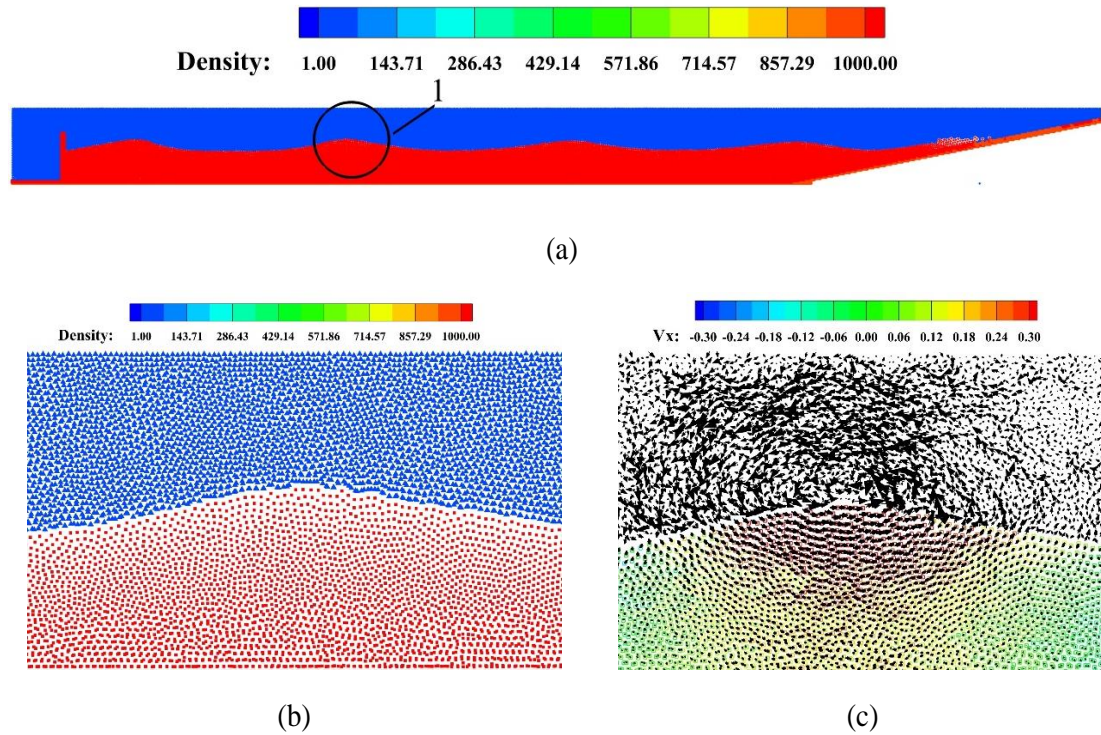


Fig. 15 Snapshot of the density for two-phase wave generation study at $t=16s$. Here (b) and (c) correspond to the enlarged of (a) and the horizontal velocity and vectors at marked 1, respectively.

3.4 Wave-structure interaction in a tank

The use of submerged barriers for coastal protection against the action of the wave motion has attracted the attentions of researchers, due to the advantage in low environmental impact. In this section, we focus on the WSI in a numerical tank using the two-phase SPH. As indicated in Fig. 11, a rigid beam-shaped submerged structure is located 2.8m from the initial piston with its bottom fixed to the tank. The height and the thickness of the structure are respectively 0.2m and 0.03m if not specified. A pressure sensor is arranged on the structure with a height of 0.2m (See Fig. 11). The second-order regular wave is generated using the Eq.23 by moving the piston. The wave parameters and other SPH simulation settings are consistent with those in the previous section if not specified. Figure 16 presents the evolution of the dimensionless pressure on the sensor of the structure for one-phase and two-phase simulations. Note that the total numbers of the particles are consistent with those in the previous section, i.e., 21900 for one-phase and 53161 for two-phase simulations with a resolution of $R=0.01m$, in which the solid particles (structure) occupy the former fluid particles. We have also obtained the one-phase pressure evolutions using *DualSPHysics* with resolutions of $R=0.01m$ and $R=0.005m$, respectively. The pressure evolutions show no obvious difference with increasing the resolution to $R=0.005m$, an indication of convergence at this level of resolution $R=0.01m$. Note that a dimensionless pressure is defined as $P^*=P/(\rho_0 g d)$ for a better comparison with the hydrostatic pressure. It is observed that the pressure on the sensor oscillates with a period of approximate 1.3s, an average dimensionless pressure of 0.6 and an approximate amplitude of 0.6 starting from $t=3s$. There is no appreciable difference between the one-phase and two-phase simulations, indicating that the effect of the air phase on the submerged structure is negligible. The two-phase wave surface, nevertheless, is observed smoother than that of the one-phase flow. Three

representative instants are captured and could be used to describe a typical periodic process as indicated in Fig.17. At $t_1=12.2s$, the pressure peak is formed by the impact of water when the wave crest passes over the structure (See Fig.17 (a), (b)). Then the pressure drops gradually as the wave crest passes through the structure ($t_2=12.6s$, see Fig.17 (c), (d)). Afterwards, a temporary backflow occurs at $t_3=13s$, causing the pressure to decay to the trough (See Fig.17 (e), (f)). Since the wave elevation after the structure is significant to assess the effectiveness of the barrier for coastal protection, we obtain the free surface evolutions at wave gauge 3 as shown in Fig.18. It is observed that the wave after the structure have a period of 1.3s, which is coincident with the theory solution when removing the submerged structure. Compared with the surface elevation of the theory, the arrangement of the structure could significantly reduce the wave height, confirming that submerged structure plays a role in coastal protection. The different structural sizes are taken into account to illustrate the effectiveness for coastal protection. As indicated in Fig.19, the wave height decreases with increasing the structure height (d_3). Increasing the thickness of the structure to $S_1=0.12m$, no evident wave height variation is observed for the structures with identical height at wave gauge 3.

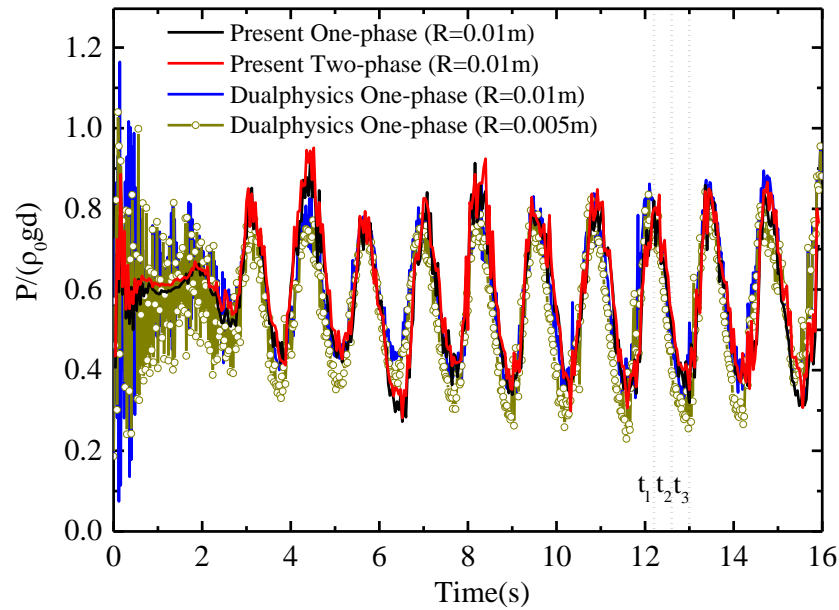
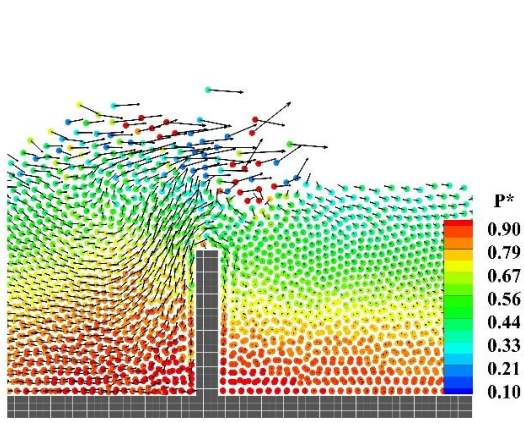
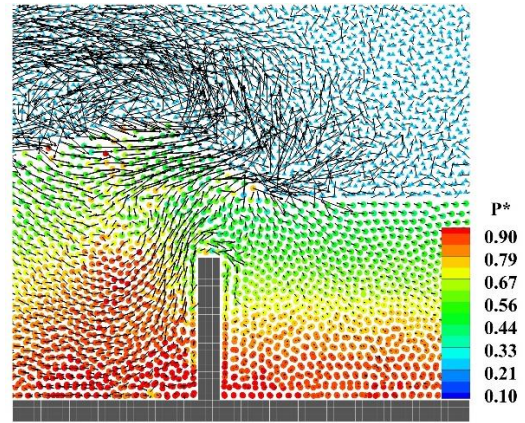


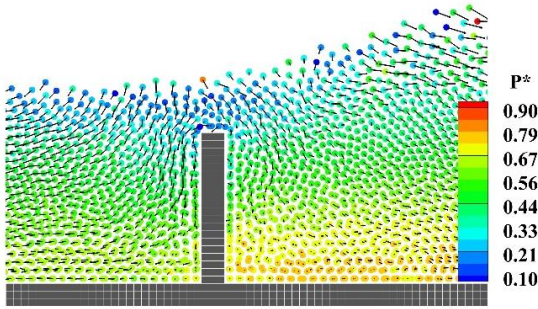
Fig. 16 Time evolution of the dimensionless pressure on the sensor of the structure for one-phase and two-phase wave generation studies.



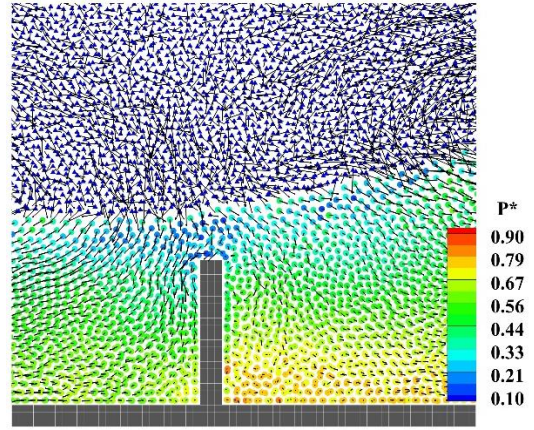
(a) One-phase flow ($t_1=12.2s$)



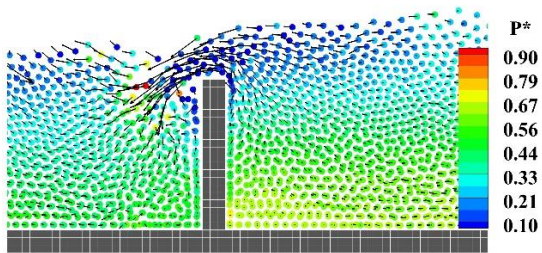
(b) Two-phase flow ($t_1=12.2s$)



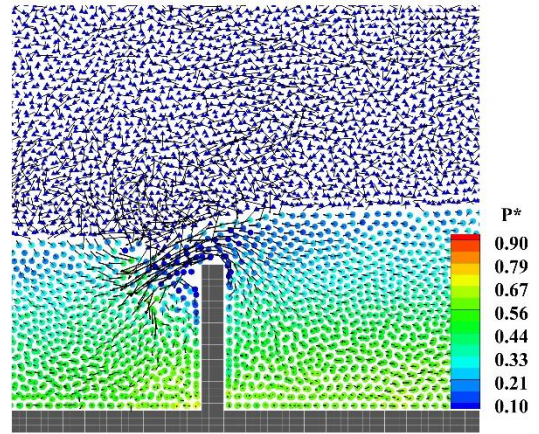
(c) One-phase flow ($t_2=12.6s$)



(d) Two-phase flow ($t_2=12.6s$)



(e) One-phase flow ($t_3=13s$)



(f) Two-phase flow ($t_3=13s$)

Fig. 17 Snapshot of the dimensionless pressure in the vicinity of the structure for one-phase and two-phase wave generation studies.

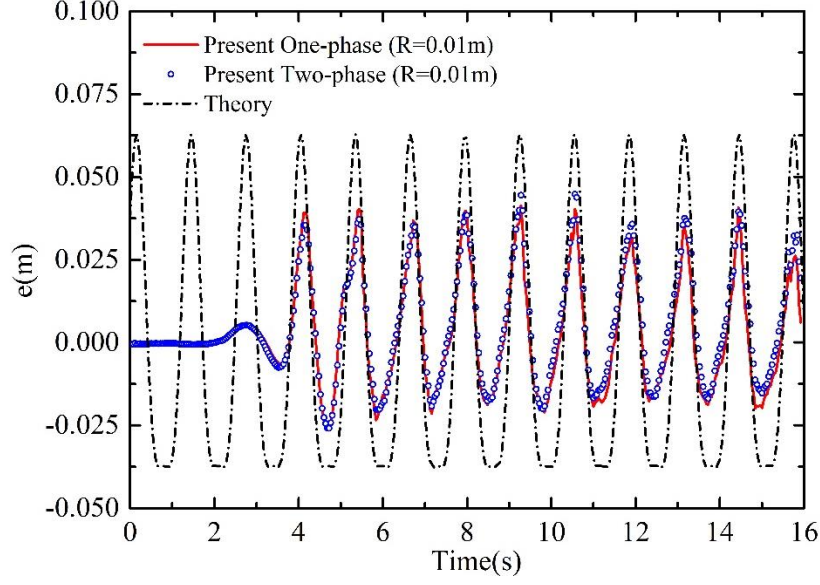


Fig 18. Free surface evolutions after the structure at wave gauge 3 for the wave generation studies.

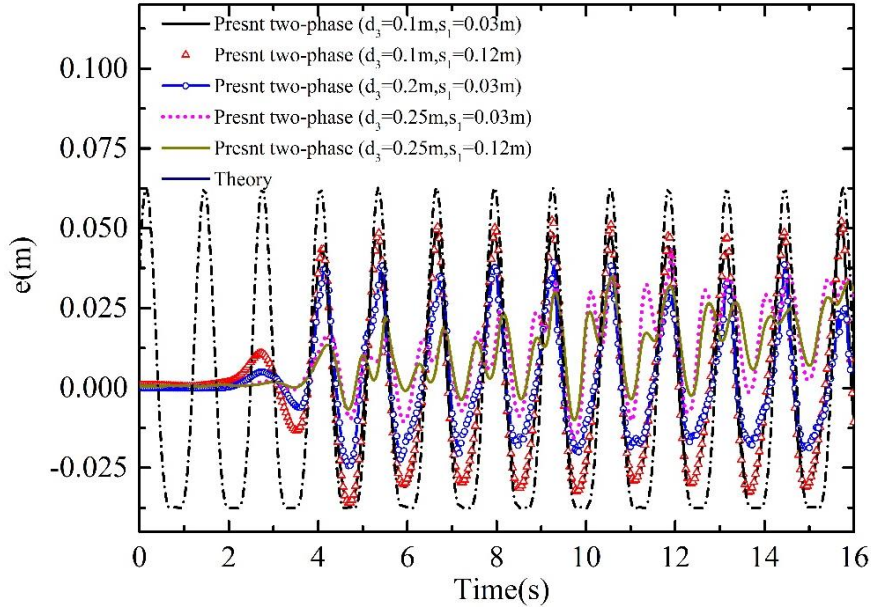


Fig 19. Free surface evolutions with different structural sizes at wave gauge 3 for the wave generation studies.

3.5 Wave interaction with a freely floating box in a tank

A freely floating box in the wave tank is tested here. This problem has been experimented and simulated using SPH model by Ren et al. [58], and Domínguez et al. [59] has presented a validation using *DualSPHysics* model. In their simulations, only water is taken into account with neglecting the effect of air phase on the floating box. Here, our two-phase SPH model is used to test this case firstly, and the 2D simulation

setup is based on the experiment and the previous simulations as indicated in Fig. 20. A freely floating box with $l=0.3\text{m}$ long, $h=0.2\text{m}$ high and a half of the water density (500kg/m^3) is initially still on the surface of the water. The box is excited by the wave with the period of $T=1.2\text{ s}$ and wave height $H_0=0.1\text{m}$ generated by a piston, thus creating its motions in the direction (surge) and perpendicular to the direction (heave) of wave propagation and the rotation (pitch) with respect to the mass center. The motion of the piston is based on the Eq. 23, generating a second order wave which is absorbed in the 1:4-sloped dissipative beach at the end. The no-slip boundary conditions are implemented on the bottom wall and the dissipative beach. Buffer 1 and buffer 2 denote the open boundaries aforementioned in the former Sections 3.3 and 3.4. Other numerical setup remains the same with those in Section 3.4 if not specified. The total particle numbers are respectively 70023 for two-phase and 32770 for one-phase simulations with a resolution of 0.01m which is recommended by Ren et al. [58]. Figs. 21-23 present a time evolution of the heave, surge and pitch for the floating box, our results show an agreement with the experimental data to a large extent, indicating that the SPH code we used has great potential in dealing with wave-floating structure interaction in multiphase (air-water) flows. Comparing the results between one-phase and two-phase simulations, the observed slight differences indicate that the one phase model is an acceptable simplification to reflect the two-phase wave-floating structure interaction problem when the air is still in the infinite field. The density and the dimensionless pressure ($P^*=P/(\rho_0 g d)$) at two typical instants (See Fig. 21) are depicted in Fig. 24. It is observed that the air-water-box interface is clearly captured, and the box is lifted up (Fig. 24 (c)) with higher pressure at the bottom of the wave tank than that when it is falling (Fig. 24 (d)).

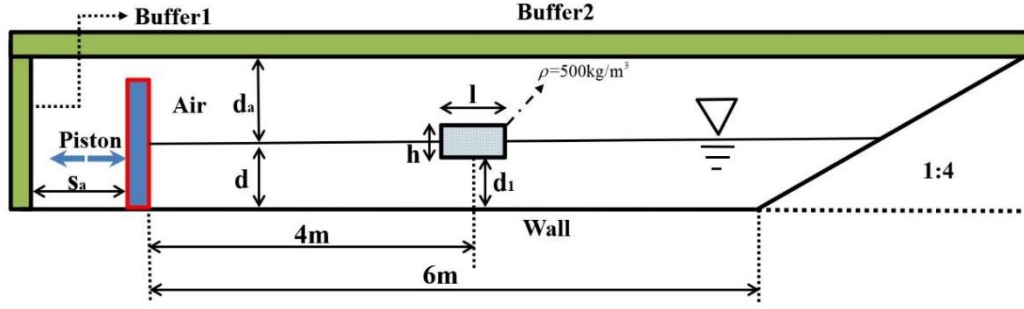


Fig. 20 Schematic of initial location for a freely floating box in the 2D two-phase wave tank.

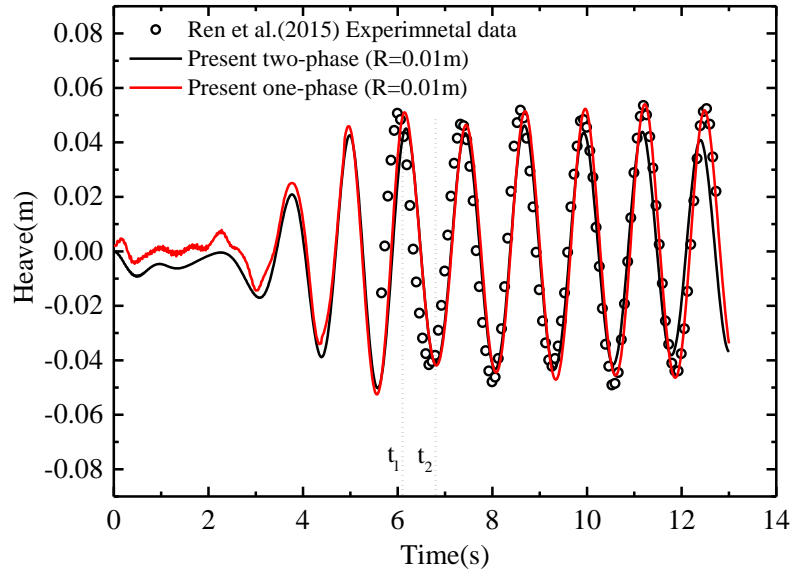


Fig. 21 Comparison between experimental (Ren et al. [58]) and numerical time evolution for the heave of the freely floating box under the action of regular waves.

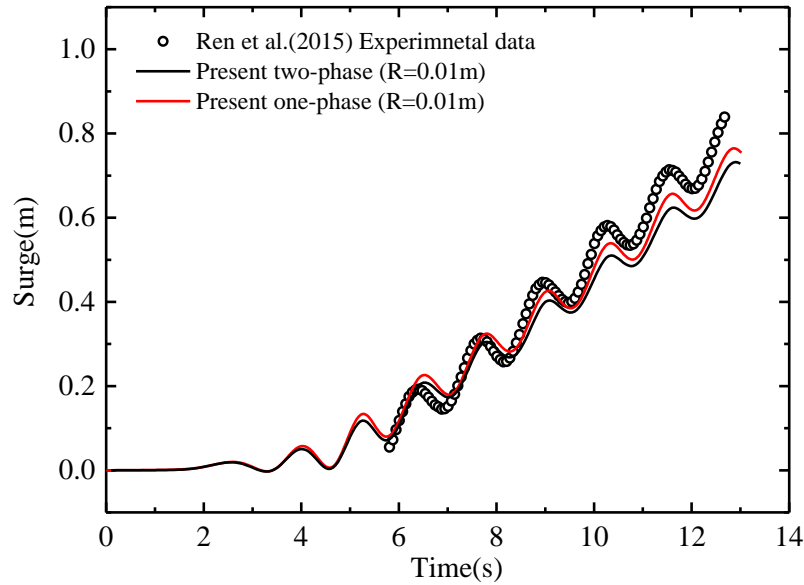


Fig. 22 Comparison between experimental (Ren et al. [58]) and numerical time evolution for the surge of the freely floating box under the action of regular waves.

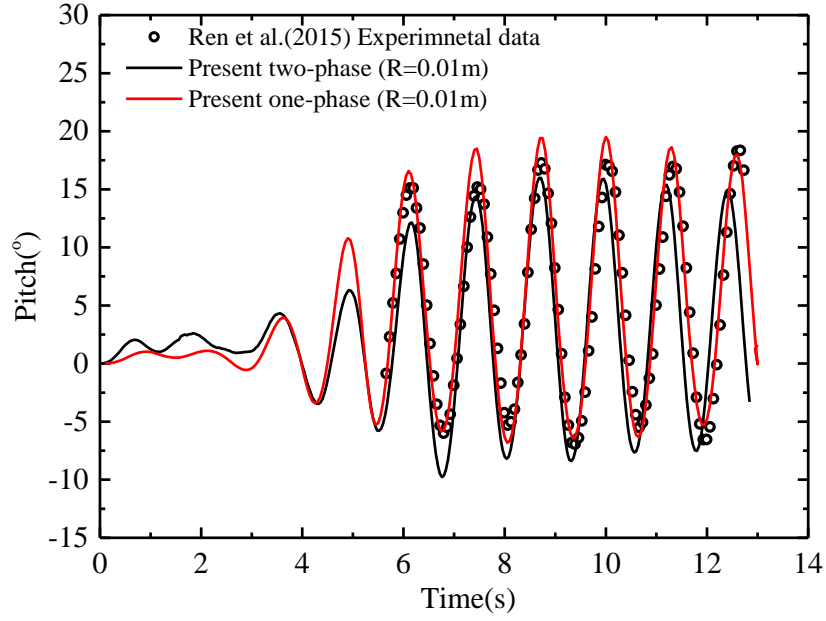


Fig. 23 Comparison between experimental (Ren et al. [58]) and numerical time evolution for the pitch of the freely floating box under the action of regular waves.

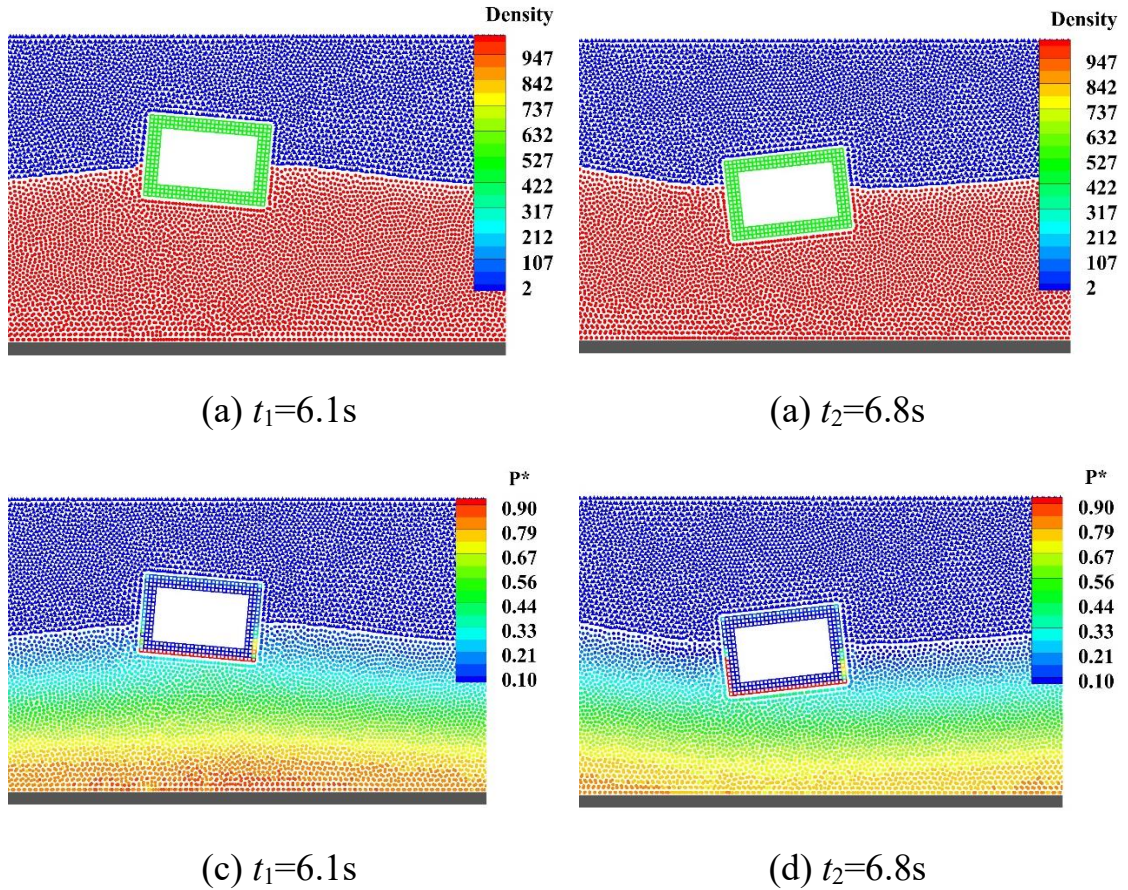


Fig. 24 Different time instants for the freely floating box under the action of regular waves. (a) and (b) density, (c) and (d) pressure.

4. Conclusions

In this paper, an SPH method is used to simulate the two-phase flows of a dam breaking, a wave making in a tank and the WSI problems, which are representative in the field of ocean engineering. For the two-phase dam breaking, it is observed that the two-phase simulation forms a smoother interface of cavity due to the local anti-extrusion of the air phase. Without the air phase, the cavity collapses as a result of pressure difference between its top and bottom. The pressure evolution of a sensor on the right wall using one- and two-phase SPH simulations are coincident with the experimental data and the existing numerical result, indicating that our numerical model could provide a reliable accuracy for this problem. To prepare the two-phase simulations for the wave making in a tank and the WSI problems, the “mirror” open boundary condition is validated using the benchmark case of flow past a circular cylinder at $Re=20$ and 200. The velocity, pressure contours obtained at the two representative Reynolds numbers do not show any discernable spurious oscillations and the periodic vortex shedding is clearly captured at $Re=200$. Meanwhile, the drag and lift coefficients, as well as the Strouhal number are comparable to those of other references, showing that the “mirror” open boundary condition implemented in our code can accurately cope with open boundary with zero pressure and velocity gradients. Based on the Biesel transfer function theory, the two-phase second order regular wave is generated by moving a piston in a tank with implementing the open boundary conditions on the top and left of the air phase. The free surface evolutions and the velocity components which we have obtained using the one- and two-phase SPH at the wave gauges match the theoretical solution and those obtained by *DualSPHysics* to a good extent. Even though the same velocity patterns and free-surface profiles are observed for the one- and two-phase simulation in a global sight, the air phase could smooth the water-air interface by complementing the particles for the calculation in the vicinity of the water surface area where the particle supporting domain is truncated for the one-phase problem. The effect of different structural sizes on the wave height after the structure is investigated, finding that the

increasing in structure height leads to a decreasing of wave elevation. On the motion of a freely floating box under the wave, our results show an agreement with the experimental data and only slight differences have been observed for the one- and two-phase simulations.

References

Data availability statement:

The data that support the findings of this study are available from the corresponding author upon reasonable request.

- [1] Fugazza, M. & Natale, L. 1992 Hydraulic design of perforated breakwaters. *J. Waterw. Port Coast. Ocean Eng.* **118**(1), 1-14.
- [2] Liu, Y., Li, Y. & Teng, B. 2007 Wave interaction with a perforated wall breakwater with a submerged horizontal porous plate. *Ocean Eng.* **34**(17-18), 2364-2373.
- [3] Huang, Z., Li, Y. & Liu, Y. 2011 Hydraulic performance and wave loadings of perforated/slotted coastal structures: A review. *Ocean Eng.* **38**(10), 1031-1053.
- [4] Lamas-Pardo, M., Iglesias, G. & Carral, L. 2015 A review of very large floating structures (VLFS) for coastal and offshore uses. *Ocean Eng.* **109**, 677-690.
- [5] Suzuki, H., Bhattacharya, B., Fujikubo, M., Hudson, D. A., Riggs, H. R., Seto, H. & Zong, Z. 2006. ISSC committee VI. 2: very large floating structures. *16th ISSC*, 394-442.
- [6] Wang, C. M. & Tay, Z. Y. 2011 Very large floating structures: applications, research and development. *Procedia Eng.*, **14**, 62-72.
- [7] Chakrabarti, S. K. (Ed.) 2005 Numerical Models in Fluid Structure Interaction, Advances in Fluid Mechanics, Vol. 42, WIT Press.
- [8] Dowell, E. H. & Hall, K. C. 2001 Modeling of fluid-structure interaction, *Annu.*

Rev. Fluid Mech. **33**,445-490.

[9] Weymouth, G. 2008 Physics and Learning Based Computational Models for Breaking Bow Waves Based on New Boundary Immersion Approaches, Ph.D. Dissertation, MIT.

[10] Weymouth, G., Dommermuth, D. G., Hendrickson, K. & Yue, D. K.P. 2006 Advances in Cartesian-grid Methods for Computational Ship Hydrodynamics, 26th Symposium on Naval Hydrodynamics, Rome, Italy, 17-22 September.

[11] Hou, G., Wang, J. & Layton, A. 2012 Numerical methods for fluid-structure interaction-a review. *Commun. Comput. Phys.* **12** (2), 337-377.

[12] Hubner, B., Walhorn, E. & Dinkler, D. 2004 A monolithic approach to fluid-structure interaction using space-time finite elements. *Comput. Meth. Appl. Mech. Eng.* **193**, 2087-2104.

[13] Ryzhakov, P. B., Rossi, R., Idelsohn, S. R. & Ōnate, E. 2010 A monolithic Lagrangian approach for fluid-structure interaction problems. *Comput. Mech.* **46**, **2010**, 883-899.

[14] Donea, J., Giuliani, S. & Halleux, J. P. 1982 An arbitrary Lagrangian-Eulerian finite element method for transient dynamic fluid-structure interactions. *Comput. Meth. Appl. Mech. Eng.* **33**(1-3), 689-723.

[15] Gerstenberger, A. & Wall, W. A. 2008 An extended finite element method/Lagrange multiplier based approach for fluid-structure interaction. *Comput. Meth. Appl. Mech. Eng.* **197**(19-20), 1699-1714.

[16] Slone, A. K., Pericleous, K., Bailey, C. & Cross, M. 2002 Dynamic fluid-structure interaction using finite volume unstructured mesh procedures. *Comput. Struct.* **80**(5-6), 371-390.

[17] Slone, A. K., Pericleous, K., Bailey, C., Cross, M. & Bennett, C. 2004 A finite volume unstructured mesh approach to dynamic fluid-structure interaction: an assessment of the challenge of predicting the onset of flutter. *Appl. Math. Model.* **28**(2), 211-239.

[18] Shi, X. & Phan-Thien, N. 2005 Distributed Lagrange multiplier/fictitious domain

method in the framework of lattice Boltzmann method for fluid-structure interactions. *J. Comput. Phys.* **206**(1), 81-94.

[19] Ouyang, Z., Lin, J. Z. & Ku, X. 2017 Hydrodynamic interactions between a self-rotation rotator and passive particles. *Phys. Fluids* **29**(10), 103301.

[20] Ouyang, Z., Lin, J. & Ku, X. 2019 Hydrodynamic interaction between a pair of swimmers in power-law fluid. *Int. J. Non-Linear Mech.* **108**, 72-80.

[21] Ouyang, Z., Lin, J. & Ku, X. 2018 Hydrodynamic properties of squirmer swimming in power-law fluid near a wall. *Rheol. Acta* **57**(10), 655-671.

[22] Ouyang, Z., Lin, J. & Ku, X. 2018 The hydrodynamic behavior of a squirmer swimming in power-law fluid. *Phys. Fluids* **30**(8), 083301.

[23] Bertevas, E., Férec, J., Khoo, B. C., Ausias, G. & Phan-Thien, N. 2018 Smoothed particle hydrodynamics (sph) modeling of fiber orientation in a 3d printing process. *Phys. Fluids* **30**(10), 103103.

[24] Tran-Duc, T., Phan-Thien, N. & Khoo, B. C. 2017 A smoothed particle hydrodynamics (SPH) study of sediment dispersion on the seafloor. *Phys. Fluids* **29**(8), 083302.

[25] Tran-Duc, T., Phan-Thien, N. & Khoo, B. C. 2018 A smoothed particle hydrodynamics (SPH) study on polydisperse sediment from technical activities on seabed. *Phys. Fluids* **30**(2), 023302.

[26] Tran-Duc, T., Phan-Thien, N. & Khoo, B. C. 2019 A three-dimensional smoothed particle hydrodynamics dispersion simulation of polydispersed sediment on the seafloor using a message passing interface algorithm. *Phys. Fluids* **31**(4), 043301.

[27] Ouyang, Z., Bertevas, E., Parc, L., Khoo, B. C., Phan-Thien, N., Férec J. & Ausias, G. A smoothed particle hydrodynamics simulation of non-isothermal fiber filled composites in a three-dimensional printing process. *Phys. Fluids* **31**, 123102.

[28] Ouyang, Z., Bertevas, E., Wang, D., Khoo, B. C., Férec, J., Ausias, G. & Phan-Thien, N. 2020 A smoothed particle hydrodynamics study of a non-isothermal and thermally anisotropic fused deposition modeling process for a fiber-filled composite. *Phys. Fluids* **32**(5), 053106.

- [29] Ye, T., Phan-Thien, N., Khoo, B. C. & Lim, C. T. 2014 Dissipative particle dynamics simulations of deformation and aggregation of healthy and diseased red blood cells in a tube flow. *Phys. Fluids* **26**(11), 111902.
- [30] Ye, T., Phan-Thien, N. & Lim, C. T. 2016 Particle-based simulations of red blood cells-A review. *J. Biomech.* **49**(11), 2255-2266.
- [31] Ye, T., Pan, D., Huang, C. & Liu, M. 2019 Smoothed particle hydrodynamics (SPH) for complex fluid flows: Recent developments in methodology and applications. *Phys. Fluids* **31**(1), 011301.
- [32] Antoci, C., Mario G. & Stefano, S. 2007 Numerical simulation of fluid-structure interaction by SPH. *Comput. Struct.* **85**(11-14), 879-890.
- [33] Lucy, L. B. 1977 A numerical approach to the testing of the fission hypothesis, *Astron. J.* **83**,1013-1024.
- [34] Gingold, R. A. & Monaghan, J. J. 1977 Smoothed particle hydrodynamics theory and application to non-spherical stars. *Mon. Not. R. Astron. Soc.* **181**, 375-389.
- [35] Ni, X. Y. & Feng, W. B. 2013 Numerical simulation of wave overtopping based on *DualSPHysics*. *Appl. Mech. Mater.* **405-408**. Trans Tech Publications Ltd, 1463-1471.
- [36] Wen, H., Ren, B., Dong, P. & Wang, Y. 2016 A SPH numerical wave basin for modeling wave-structure interactions. *Appl. Ocean. Res.* **59**, 366-377
- [37] Altomare, C., Domínguez, J. M., Crespo, A. J. C., González-Cao, J., Suzuki, T., Gómez-Gesteira, M., & Troch, P. 2017 Long-crested wave generation and absorption for SPH-based *DualSPHysics* model. *Coast. Eng.* **127**, 37-54.
- [38] Meringolo, D. D., Francesco A., & Paolo V. 2015 SPH numerical modeling of wave-perforated breakwater interaction. *Coast. Eng.* **101**, 48-68.
- [39] Huang, C., Zhang, D. H., Si, Y. L., Shi, Y. X. & Lin, Y. G. 2018 Coupled finite particle method for simulations of wave and structure interaction. *Coast. Eng.* **140**, 147-160.
- [40] Yang, X., Liu, M., Peng, S., & Huang, C. 2016 Numerical modeling of dam-break flow impacting on flexible structures using an improved SPH-EBG

method. *Coast. Eng.* **108**, 56-64.

[41] Antuono, M. Colagrossi, A. & Marrone, S. 2012 Numerical diffusive terms in weakly-compressible SPH schemes. *Comput. Phys. Commun.* **183**, 2570-2580.

[42] Hu, X. Y. & Adams, N. A. 2007 An incompressible multi-phase SPH method. *J. Comput. Phys.* **227**(1), 264-278.

[43] Monaghan, J. J. 1992 Smoothed particle hydrodynamics. *Annu. Rev. Astron. Astrophys.* **30**(1), 543-574.

[44] Morris, J. P., Fox, P. J. & Zhu, Y. 1997 Modeling low Reynolds number incompressible flows using SPH. *J. Comput. Phys.* **136**(1), 214-226.

[45] Adami, S., Hu, X. Y. & Adams, N. A. 2012 A generalized wall boundary condition for smoothed particle hydrodynamics. *J. Comput. Phys.* **231**(21), 7057-7075.

[46] Tafuni, A., Domínguez, J. M., Vacondio, R. & Crespo, A. J. C. 2018 A versatile algorithm for the treatment of open boundary conditions in smoothed particle hydrodynamics GPU models. *Comput. Meth. Appl. Mech. Eng.* **342**, 604-624.

[47] Liu, M. B. & Liu, G. R. 2006 Restoring particle consistency in smoothed particle hydrodynamics. *Appl. Numer. Math.* **56** (1), 19-36.

[48] Verlet, L. 1967 Computer "experiments" on classical fluids. I. Thermodynamical properties of Lennard-Jones molecules. *Phys. Rev.* **159**(1), 98.

[49] Gong, K., Shao, S., Liu, H., Wang, B. & Tan, S. K. 2016 Two-phase SPH simulation of fluid-structure interactions. *J. Fluids Struct.* **65**, 155-179.

[50] Chen, Z., Zong, Z., Liu, M. B., Zou, L., Li, H. T. & Shu, C. 2015 An SPH model for multiphase flows with complex interfaces and large density differences. *J. Comput. Phys.* **283**, 169-188.

[51] Colagrossi, A. & Landrini, M. 2003 Numerical simulation of interfacial flows by smoothed particle hydrodynamics. *J. Comput. Phys.* **191**, 448-475.

[52] Tritton, D.J. 1959 Experiments on the flow past a circular cylinder at low Reynolds numbers. *J. Fluid Mech.* **6**, 547-567.

[53] Marrone, S., Colagrossi, A., Antuono, M., Colicchio, G. & Graziani, G. 2013 An accurate SPH modeling of viscous flows around bodies at low and moderate Reynolds

numbers. *J. Comput. Phys.* **245**, 456-475.

[54] Le, D. V., Khoo, B. C. & Lim., K. M. 2008 An implicit-forcing immersed boundary method for simulating viscous flows in irregular domains. *Comput. Meth. Appl. Mech. Eng.* **197**(25-28), 2119-2130.

[55] Negi, P., Ramachandran, P. & Haftu, A. 2020 An improved non-reflecting outlet boundary condition for weakly-compressible SPH. *Comput. Meth. Appl. Mech. Eng.* **367**, 113119.

[56] Biesel, F. & Suquet, F. 1951 Etude theorique d'un type d'appareil a la houle. *La Houille Blanche*. 6e Ann, **2**, 152-165.

[57] Madsen, O.S. 1971 On the generation of long waves. *J. Geophys. Res.* **76**, 8672-8683.

[58] Ren, B., He, M., Dong, P., & Wen, H. 2015 Nonlinear simulations of wave-induced motions of a freely floating body using WCSPH method. *Appl. Ocean. Res.* **50**, 1-12.

[59] Domínguez, J. M., Crespo, A. J., Hall, M., Altomare, C., Wu, M., Stratigaki, V., Troch, P. Cappietti, L. & Gómez-Gesteira, M. 2019 SPH simulation of floating structures with moorings. *Coast. Eng.* **153**, 103560.